International Journal of Biological Macromolecules 259 (2024) 129210

Contents lists available at ScienceDirect

International Journal of Biological Macromolecules

journal homepage: www.elsevier.com/locate/ijbiomac

Reduced graphene oxide–reinforced tricalcium phosphate/gelatin/chitosan light-responsive scaffolds for application in bone regeneration

Cátia S.D. Cabral [a], Duarte de Melo-Diogo [a], Paula Ferreira [b], André F. Moreira [a,c,*], Ilídio J. Correia [a,d,*]

[a] CICS-UBI – Centro de Investigação em Ciências da Saúde, Universidade da Beira Interior, Covilhã, Portugal
[b] Instituto Politécnico de Coimbra, Instituto de Investigação Aplicada, Coimbra, Portugal
[c] CPIRN-UDI/IPG – Centro de Potencial e Inovação em Recursos Naturais, Unidade de Investigação para o Desenvolvimento do Interior, Instituto Politécnico da Guarda, Guarda, Portugal
[d] CIEPQPF – Departamento Engenharia Química, Universidade de Coimbra, Coimbra, Portugal

ARTICLE INFO

Keywords:
3D scaffolds
Bone tissue engineering
Rapid prototyping
Chitosan
Reduced graphene oxide
Near-infrared radiation

ABSTRACT

Bone is a mineralized tissue with the intrinsic capacity for constant remodeling. Rapid prototyping techniques, using biomaterials that mimic the bone native matrix, have been used to develop osteoinductive and osteogenic personalized 3D structures, which can be further combined with drug delivery and phototherapy. Herein, a Fab@Home 3D Plotter printer was used to promote the layer-by-layer deposition of a composite mixture of gelatin, chitosan, tricalcium phosphate, and reduced graphene oxide (rGO). The phototherapeutic potential of the new NIR-responsive 3D_rGO scaffolds was assessed by comparing scaffolds with different rGO concentrations (1, 2, and 4 mg/mL). The data obtained show that the rGO incorporation confers to the scaffolds the capacity to interact with NIR light and induce a hyperthermy effect, with a maximum temperature increase of 16.7 °C after under NIR irradiation (10 min). Also, the increase in the rGO content improved the hydrophilicity and mechanical resistance of the scaffolds, particularly in the 3D_rGO4. Furthermore, the rGO could confer an NIR-triggered antibacterial effect to the 3D scaffolds, without compromising the osteoblasts' proliferation and viability. In general, the obtained data support the development of 3D_rGO for being applied as temporary scaffolds supporting the new bone tissue formation and avoiding the establishment of bacterial infections.

1. Introduction

Bone is a structurally complex and mineralized connective tissue with the intrinsic capacity for constant remodeling [1–3]. Due to its rigid structure, bone is involved in different pivotal functions in the human body, such as locomotion and protection of vital organs, as well as in the hematopoiesis and maintenance of homeostasis [2–4]. Despite the bone's self-regenerative capacity, during the individual's lifetime injuries or diseases can arise, compromising the native structure and functions of the bone. To address these conditions, the gold standard treatments, such as autografts, allografts, or xenografts, have been applied in the clinic. Nevertheless, these classic therapeutic approaches still report several limitations, namely the restricted availability, the development of new lesions, and the possibility of immunological rejection or disease transmission [5,6]. In this regard, the tissue engineering area has been exploring the utilization of biomaterials, cells, and/or bioactive molecules for designing new solutions for the treatment of bone injuries [7].

Different biomimetic strategies have been applied to develop bone-like structures, namely using rapid prototyping for producing 3D structures personalized to the patient's injury [8–10]. Moreover, 3D printed scaffolds can also be engineered for reproducing the native extracellular matrix of bone as well as enhancing osteoinductivity and osteoconductivity [11]. To accomplish that, scientists often combine biomaterials that mimic the inorganic and organic components of the bone matrix. Ceramics such as hydroxyapatite and tricalcium phosphate (TCP) provide enhanced mechanical properties, whereas polymers such as collagen, silk fibroin, chitosan, and gelatin, confer elasticity and enhance the bioactivity to the temporary 3D supports [12,13]. However, several of these composite formulations fail to meet all the requirements for an *in vivo* application, namely due to poor mechanical and physicochemical properties [14].

* Corresponding authors at: CICS-UBI – Centro de Investigação em Ciências da Saúde, Universidade da Beira Interior, Covilhã, Portugal
E-mail addresses: afmoreira@fcsaude.ubi.pt (A.F. Moreira), icorreia@ubi.pt (I.J. Correia).

https://doi.org/10.1016/j.ijbiomac.2024.129210
Received 17 October 2023; Received in revised form 7 December 2023; Accepted 1 January 2024
Available online 5 January 2024

Reduced graphene oxide has been recently explored in bone regeneration applications due to the high fracture strength, large specific surface area, atomic structure stability, and biocompatibility, which can confer to the 3D structures improved physicochemical, mechanical, and antibacterial properties [15–21]. Moreover, to enhance the effectiveness of osteogenesis, rGO can also be used as a photothermal agent in hyperthermia strategies to improve the regeneration of bone tissue. Photothermal therapy (PTT) explores the conversion of light, usually near-infrared (NIR) light with a wavelength range of 700–1200 nm, into heat. The localized temperature increase can be effective in preventing infections since temperatures above 45 °C start to affect the integrity of the bacterial cell membrane and inhibit bacterial proliferation [22,23]. Graça and colleagues reported that the increase in the rGO concentration from 100 μg/mL to 200 μg/mL on CS-based hydrogels enhanced the antibacterial efficacy. In the presence of NIR light, the CS-based hydrogels containing 200 μg/mL of rGO mediated the decrease in the bacteria viability from 88 % to 56 % and 88 % to 5 % for *E. coli* and *S. aureus*, respectively [24]. In a similar approach, Li et al. developed a rGO enriched nano-hydroxyapatite scaffold (nHA-rGO) to evaluate the impact of the photothermal effect simultaneously in cancer therapy and bone regeneration. The authors verified that the nHA-rGO scaffold could promote the proliferation and differentiation of rat bone marrow stem cells in osteogenic lineages, as evidenced by the upregulated ALP activity, and simultaneously inhibit the tumor growth by promoting the death of osteosarcoma cells, when irradiated with NIR light (808 nm, 1 W/cm^2, 20 min) [25].

Herein, rGO was explored to create a 3D scaffold with the capacity to prevent bacterial infections and enhance the regeneration process of bone fractures. For that purpose, a Fab@Home 3D Plotter printer was used to produce layer-by-layer the 3D scaffolds based on the composite mixture of tricalcium phosphate (TCP), gelatin (Gel), chitosan (CH), and rGO. TCP is a ceramic with bioactive and osteoconductive properties and was used to reproduce the inorganic component of bone [26,27]. In turn, Gel and CH were combined to reproduce the organic phase of this tissue, providing elasticity, biocompatibility, and bioadhesivity [15,28,29]. Moreover, the incorporation of rGO at concentrations of 1, 2, and 4 mg/mL was tested to further evaluate the impact of this nanomaterial in the physicochemical and biological properties, *i.e.*, biocompatibility, osteogenic, and antibacterial capacity of the scaffolds.

2. Materials and methods

2.1. Materials

Acetic acid was obtained from Pronalab (Barcelona, Spain). Lysozyme from the chicken egg was acquired from Alfa Aesar (Haverhill, MA, USA). Alizarin Red S, alkaline phosphatase, chitosan medium molecular weight (190 000–310 000 Da; degree of deacetylation: 83.35 % ± 0.23), Dulbecco's modified Eagle's medium (DMEM-F12), diethanolamine, ethylenediaminetetraacetic acid (EDTA), gelatin 160 bloom, glutaraldehyde 25 % (*v*/v), hydrochloric acid (HCl), LB broth, paraformaldehyde (PFA), phosphate buffered saline solution (PBS), *p*-Nitrophenylphosphate (pNPP), resazurin, sodium hydroxide (NaOH), sodium tripolyphosphate (TPP), triton X-100 and trypsin were acquired from Sigma Aldrich (Sintra, Portugal). Graphene oxide (GO) was acquired from NanoPoz (Umultowska Poznan, Wielkopolska). Propidium Iodide buffer was purchased from Life Technologies (Maryland, USA). Tricalcium phosphate (TCP) was bought from Panreac (Barcelona, Spain). L-Ascorbic acid (LAA) was obtained from Fisher Scientific (Porto Salvo, Portugal). Normal human osteoblast (hOB; 406-05f) cryopreserved cells were acquired from Cell Applications, Inc. (San Diego, USA). *Staphylococcus aureus* clinical isolate (*S. aureus*; ATCC 25923) and *Escherichia coli DH5a* (*E. coli*) were used to assess the scaffolds' antibacterial properties. Fetal bovine serum was obtained from Biochrom AG (Berlin, Germany). Double deionized and filtered water was obtained using a Milli-Q Advantage A10 ultrapure Water Purification System (0.22 μm filtered; 18.2 MΩ/cm at 25 °C).

2.2. Methods

2.2.1. Production of 3D_rGO scaffolds

GO was combined with a mixture of TCP and Gel/CH, at an approximated ceramic/polymer *w*/w ratio of 80/20, to form the composite mixture used in the production of 3D_rGO scaffolds, by adapting a protocol reported by [15]. Initially, a dialysis (14 kDa molecular weight cut-off membrane, water) was performed for 3 days to purify the GO solution. Then, the GO was sonicated to produce the nanosized material incorporated in the scaffolds. Dynamic Light Scattering (DLS) technique was used to determine the mean size and size distribution of GO, using a Zetasizer Nano ZS (Malvern Instruments Ltd., Worcestershire, UK).

The composite mixture was prepared by mixing 15 mL of CH 5 % (*w*/*v*, in acetic acid 1 % *v*/v), 1 mL Gel 1 % (w/v, in water). Then, TCP (4.8 g) and GO (final concentration of 1, 2, and 4 mg/mL) were added and the solution was homogenized with an X10/25 Ultra-turrax for 30 min. Afterward, a syringe (10 mL Luer Lock) was loaded with the TCP/Gel/CH/GO solution and the scaffolds were extruded layer-by-layer using a Fab@Home 3D printer. The printing process was conducted by converting the 3D digital model (CAD file) to STL. Then, the scaffolds were produced through a layer-by-layer fabrication process in the Fab@home v0.23. The *in situ* green reduction of the GO present in the scaffolds was attained by immersing them in a LAA solution (10 mM), at 40 °C for 24 h (30 rpm) [15]. Furthermore, the crosslinking of the chitosan's positively charged groups was achieved by immersing in a sodium tripolyphosphate (TPP) solution (10 % (*w*/*v*)), for 24 h. Finally, the resulting scaffolds (3D_rGO1, 3D_rGO2, 3D_rGO4) were dried at room temperature (RT). A control group without GO and undergoing the *in situ* reduction step was also produced for comparative purposes.

2.2.2. Characterization of the 3D scaffolds' morphology

The surface and morphology of the scaffolds were analyzed using a Scanning Electron Microscopy (SEM). Samples were introduced on aluminum stubs and fixed with araldite glue. Before analysis, a gold coating was applied to the scaffolds using a Quorum Q150RES sputter coater (Quorum Technologies, UK). The Hitachi S-3400 N scanning electron microscope (Hitachi, Japan) was operated at an acceleration voltage of 20 kV and the images were acquired at different magnifications.

2.2.3. Evaluation of the physicochemical properties of the scaffolds

2.2.3.1. Attenuated total reflectance-Fourier transform infrared spectroscopy. To evaluate the scaffolds' physicochemical composition, powdered samples were placed on the diamond window of a Nicolet iS10 FTIR spectrophotometer (Thermo Scientific, Waltham, MA, USA). The Attenuated Total Reflectance-Fourier Transform Infrared Spectroscopy (ATR-FTIR) spectra were acquired in the region of 400 to 4000 cm^{-1}, with a spectral resolution of 32 cm^{-1}, and an average of 128 scans. The raw materials were also analyzed for comparative purposes.

2.2.3.2. Evaluation of scaffolds' photothermal capacity. The photothermal capacity of 3D_rGO scaffolds was evaluated by adapting a protocol described in the literature [30]. Briefly, the scaffolds immersed in water were irradiated for 10 min with a NIR laser (808 nm, 1.7 W/cm^2) and the temperature variation was monitored using a thermocouple thermometer. The laser was placed at 100 cm to the plate, irradiation angle of 90°, and the focus point was on the center of the well of the plate. The control group refers to the temperature variation of water irradiated with the NIR light.

2.2.3.3. Contact angle measurements. A sessile drop method of water contact angle (WCA) method was used to evaluate the scaffolds'

hydrophobicity. Briefly, 10 μL of double deionized water were automatically dispersed onto the sample's surface and the contact angle was measured by a Dataphysics OCA 20 contact angle analyzer (Dataphysics Instruments, Filderstadt, Germany). The mean static contact angle was obtained from ten measurements on different surface points of the scaffolds.

2.2.3.4. Analysis of the scaffolds' mechanical properties. The mechanical properties of the scaffolds ($n = 5$) were assessed through compressive assays, as described in the literature [31]. To perform the compressive assays, the scaffolds were placed in a Shimadzu AG-X Tensile Testing Machine (Tokyo, Japan) operated at RT with a crosshead speed of 3 mm/min and a load cell of 5 kN. Compressive strength was calculated using Eq. (1):

$$\text{Compressive strength} = \frac{F}{w \times l} \quad (1)$$

F refers to the load at the time of fracture, whereas the w and l are the scaffolds' width and length, respectively.

The stress-strain relation was used to calculate the Young Modulus, Eq. (2):

$$\text{Young Modulus} = \frac{C_s}{(dL/L)} \quad (2)$$

C_S is the compressive strength of the scaffold, dL refers to the elongation or compression (*i.e.* change in length) and L corresponds to the original length of the scaffold.

2.2.3.5. Evaluation of scaffolds' porosity. The liquid displacement method was utilized to determine the total porosity of the 3D scaffolds, adapting a protocol described before [31,32]. EtOH was selected as solvent since it can penetrate the scaffold's structure with minimal structural changes, *i.e.*, swelling and shrinkage [32].

For that purpose, scaffolds with a known weight and dimensions were immersed in EtOH. One group of scaffolds was subjected to 10 min of irradiation with NIR light (808 nm, 1.7 W/cm^2), as described above. After 48 h, all scaffolds (*i.e.*, irradiated (W/NIR) and non-irradiated (W/O NIR)) were weighted and the porosity was calculated using the Eq. (3):

$$\text{Porosity } (\%) = \frac{W_w - W_d}{D_{EtOH} \times V_{scaffold}} \times 100 \quad (3)$$

W_w and W_d refer to the wet and dry weights, respectively. D_{EtOH} corresponds to the density of EtOH at RT and $V_{scaffold}$ is the scaffold volume.

The surface macroporosity of the scaffolds was quantified through the individual measurement of the macropores using the *ImageJ* software.

2.2.3.6. Evaluation of the swelling profile of the scaffolds. The scaffolds' swelling capacity was evaluated following a protocol described in the literature [15]. Succinctly, scaffolds ($n = 5$) were incubated at 37 °C in a phosphate-buffered saline (PBS) solution for 48 h at 60 rpm. At 24 h of incubation, a group of scaffolds was irradiated for 10 min with a NIR laser (808 nm, 1.7 W/cm^2), as described above. At predetermined intervals, irradiated scaffolds (W/NIR) and non-irradiated (W/O NIR) scaffolds were recovered, weighted, and re-immersed in the PBS solution. The scaffolds' swelling was then calculated using Eq. (4):

$$\text{Swelling } (\%) = \left(\frac{W_t - W_0}{W_0}\right) \times 100 \quad (4)$$

where W_t and W_0 represent the scaffolds' final and initial weight, respectively.

2.2.3.7. Analysis of the scaffolds' biodegradation profile. The degradation profile of the scaffolds was assessed in the presence or absence of NIR light [33,34]. To accomplish that, scaffolds ($n = 3$) were incubated, at 37 °C, in a PBS solution (13.6 mg/L of lysozyme) for 21 days at 60 rpm. At 24 h of incubation, a group of scaffolds were subjected to irradiation with a NIR laser (808 nm, 1.7 W/cm^2) for 10 min, as described in Section 2.2.3.2.

During the assay, the solutions were replaced periodically for guaranteeing the activity of the enzyme. For determining the weight loss (Eq. (5)), irradiated scaffolds (W/NIR) and non-irradiated (W/O NIR) scaffolds were recovered, frozen at −80 °C, freeze-dried, and weighed.

$$\text{Weight loss } (\%) = \left(\frac{W_i - W_f}{W_i}\right) \times 100 \quad (5)$$

W_i and W_f refer to the initial weight and weight of the scaffold at time t, respectively.

2.2.3.8. In vitro biomineralization assay. The *in vitro* bioactivity was evaluated by immersing the scaffolds in a SBF solution, at 37 °C for 7 and 21 days. The SBF solution presented a pH of 7.4 and ion concentration mimicking that of human blood plasma, *i.e.*, 142.0 mM Na^+, 5 mM K^+, 1.5 mM Mg^{2+}, 2.5 mM Ca^{2+}, 147.8 mM Cl^-, 4.2 mM HCO_3^-, 1.0 mM HPO_4^{2-}, and 0.5 mM SO_4^{2-} [35].

After incubation in SBF solution at 37 °C, a group of scaffolds was subjected to irradiation with a NIR laser (808 nm, 1.7 W/cm^2) for 10 min (as described in Section 2.2.3.2). At each timepoint, irradiated (W/NIR) and non-irradiated (W/O NIR) scaffolds were recovered and dried. The nucleation of apatite layers on the scaffolds' surface was assessed by SEM analysis.

2.2.4. Evaluation of the scaffolds' biological properties

2.2.4.1. Characterization of the scaffolds cytocompatibility in contact with hOB cells. The scaffolds' cytocompatibility was evaluated towards hOB cells through the resazurin assay, comparing the effect of the irradiation with the NIR laser [15,36]. The hOB cells were cultured in 96-well plates (10×10^3 cells/well) and incubated for 24 h. Then, the cells were incubated with the scaffolds and the selected groups were subjected to irradiation with NIR laser (808 nm, 1.7 W/cm^2) for 10 min, as described in Section 2.2.3.2.

At 1 and 7 days of incubation, the medium was removed and 110 μL of fresh medium containing resazurin (10 μL) were added following incubation for 4 h in the dark (37 °C, 5 % CO_2). Then, the cell viability was assessed by determining the amount of produced resorufin by fluorescence ($\lambda_{ex} = 545$ nm and $\lambda_{em} = 590$ nm) using Spectramax Gemini EM spectrofluorometer (Molecular Devices LLC, CA, USA). Cells incubated only with media were used as the negative control (K^-), while cells exposed to EtOH (70 %) were used as the positive control (K^+).

2.2.4.2. Characterization of cell adhesion at the surface of the scaffolds. The osteoblasts' adhesion at the scaffolds' surface was monitored by SEM [15]. For this purpose, hOB cells were cultured (40×10^3 cells/well) on the surface of the scaffolds and incubated, with or without NIR irradiation (808 nm, 1.7 W/cm^2, 10 min), as described in Section 2.2.3.2, for 3 days. Then, the scaffolds were recovered and incubated in glutaraldehyde (2.5 % (*v*/v)) for 30 min, followed by freezing and freeze-drying. Then, the samples were mounted on alluminium stubs and analyzed in the SEM microscope.

2.2.4.3. Confocal microscopic analysis. The hOB spreading within the scaffolds was observed, with or without NIR irradiation (808 nm, 1.7 W/cm^2, 10 min), through confocal laser scanning microscopy (CLSM). The hOB cells (20×10^3 cells/well) were seeded in the scaffolds' surface for 3 days. Then, the media was removed and the samples were washed with PBS, followed by fixation with paraformaldehyde (PFA, 4 % (*w*/*v*), for 15 min) [15]. For the cell staining, the samples were incubated treated with Triton X-100 (1 % (*v*/v) and incubated with propidium iodide (PI,

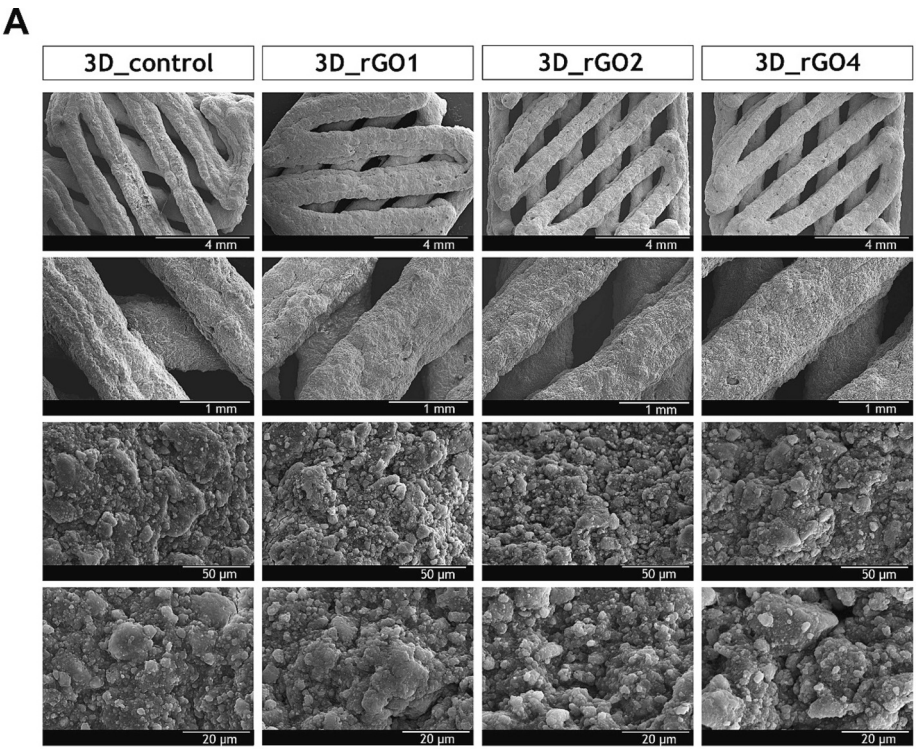

Fig. 1. SEM images (at different magnifications) showing the morphology and surface topography of the scaffolds.

15 mM) for labelling the cell nucleus. A Zeiss LSM 710 laser scanning confocal microscope (Carl Zeiss SMT Inc., USA) was used to acquire the fluorescence images and *Z*-stacks were also obtained for creating the 3D reconstructions using the Zeiss Zen 2010.

2.2.4.4. Alizarin Red S (ARS) staining. The scaffolds' ability to stimulate hOB cells to accumulate calcium was assessed using the ARS staining method, following a protocol previously described in the literature [15,37,38]. Briefly, hOB cells were cultured (10×10^2 cells/well in 12-well plates) with the scaffolds ($n = 6$). Then, a group of cells incubated with scaffolds was irradiated with a NIR laser (808 nm, 1.7 W/cm^2) for 10 min (as described in Section 2.2.3.2). Upon reaching 14 days of incubation, PFA (4 % (*w/v*)) was used to promote the fixation of the samples, followed by staining with ARS (1 mL, 40 mM, pH = 4.1–4.3). Subsequently, the excess of ARS was removed by washing with double deionized H_2O. Afterward, the samples were incubated for 30 min under agitation with acetic acid (1 mL; 10 % (*v/v*)), heated to 85 °C (10 min), and cooled down in ice for 5 min. The obtained solution was centrifuged (14,000 *g*, 25 min, at RT) and the supernatant was neutralized with ammonium hydroxide (200 µL; 10 % (*v/v*)). Then, the absorbance at 405 nm was measured using a microplate reader (Biorad xMark microplate spectrophotometer).

2.2.4.5. Alkaline phosphatase (ALP) activity. The ALP activity of hOB seeded with scaffolds was assessed as described in the literature [39,40]. The hOB cells were cultured (10×10^2 cells/well in 12-well plates) with the scaffolds ($n = 6$), for 7 days, with or without NIR laser irradiation (808 nm, 1.7 W/cm^2, 10 min), as described in Section 2.2.3.2. At the predetermined intervals, Triton X-100 (1 % (v/v), 1 mL) was used to permeabilize the cells. Then, the cell-containing scaffolds were detached from the culture plate, using a cell scrapper, and the remaining solution was transferred into microcentrifuge tubes. Thereafter, the recovered cell-containing scaffolds were submitted to a freeze-thaw cycle and sonicated for 15 min. Afterward, the samples were centrifuged (14,000 *g*, 15 min, at RT) and 20 µL of the supernatant were reacted with 60 µL of a substrate solution (0.2 % *p*-Nitrophenylphosphate (pNPP) (*w/v*) in diethanolamine-HCl (1 M, pH 9.8)) for 45 min, at 37 °C, in the dark. Subsequently, 80 µL of the stop solution (NaOH (2 M) containing EDTA (0.2 mM)) was added to the samples, and the production of *p*-nitrophenol (indicator of the ALP activity) was assessed using a Biorad xMark microplate spectrophotometer to measure the absorbance at 405 nm.

2.2.5. Evaluation of the scaffolds' antibacterial activity

The effect of NIR irradiation on scaffolds' antibacterial activity was evaluated on *S. aureus* and *E. coli*, Gram-positive and Gram-negative model bacteria, using a resazurin assay [41]. In brief, bacteria medium (1×10^8 colony-forming units (CFU)/mL) was incubated at a 96-well plate in the presence of the 3D scaffolds. Afterward, a group was subjected to treatment with NIR laser (808 nm, 1.7 W/cm^2) for 10 min (as described in Section 2.2.3.2). Then, the medium (100 µL) was recovered and incubated with resazurin (20 µL) for 4 h in the dark (37 °C, 5 % CO_2). The bacteria viability was assessed by measuring the fluorescence of the produced resorufin ($\lambda_{ex} = 545$ nm and $\lambda_{em} = 590$ nm) using a Spectramax Gemini EM spectrofluorometer (Molecular Devices LLC, CA, USA). Bacteria incubated only with media were used as the negative control (K^-), while bacteria cultured with antibiotic-antimycotic solution (amphotericin B, penicillin, streptomycin) were used as the positive control (K^+).

2.2.6. Statistical analysis

One-way analysis of variance (ANOVA) with the Newman-Keuls *post hoc* test was used for the data analysis. A p value lower than 0.05 ($p < 0.05$) was considered statistically significant.

3. Results and discussion

3.1. Characterization of the morphology of the scaffolds

Herein, the 3D scaffolds were produced using a general 3D model with stacked layers that have a rotation of 45° clockwise upon each layer printing cycle. This organization confers a homogenous distribution of pores throughout the scaffolds' structure and originates an

interconnected pore network that is beneficial for the biological performance of the scaffolds without compromising its mechanical stability [42,43].

The 3D scaffolds were composed of a mixture mimicking the natural composition of the bone matrix (*i.e.,* 20–30 % organic and 70–80 % inorganic) and using a layer-by-layer methodology. The TCP is a ceramic that mimics the bone's inorganic phase and confers mechanical strength and osteogenic effect to the scaffolds. In turn, Gel and CH due to their biocompatibility and biodegradability were selected as replacements for the organic phase. Moreover, both Gel and CH are well-known by their bioadhesive capacity and CH further shows an intrinsic antibacterial effect. Furthermore, different concentrations of nanosized rGO (Fig. S1) were incorporated in the composition of the 3D printed mixture, final concentration of 1, 2, or 4 mg/mL. This nanomaterial can improve the mechanical, osteogenic, and antibacterial properties of the scaffolds, as well as act as a photothermal agent in hyperthermia strategies to enhance bone regeneration. The 3D printed scaffolds were submitted to an *in situ* GO reduction process mediated by L-ascorbic acid (24 h, 40 °C) to obtain 3D_rGO scaffolds, as previously described by [15]. Finally, the 3D_control and 3D_rGO scaffolds were cross-linked in a TPP solution and air-dried.

The morphology of the scaffolds surface was examined by SEM (Fig. 1). The images demonstrate that 3D_rGO scaffolds, with different concentrations of rGO, have a similar architecture and present a rough surface with irregularities, which was also observed in the 3D_control scaffolds. The production of rough and irregular surfaces due to the existence of more anchorage points has been associated to an enhanced osteogenesis, which promotes protein adsorption and favors the cells' attachment and proliferation [44].

3.2. Analysis of the scaffolds' physicochemical properties

3.2.1. Attenuated total reflectance-Fourier transform infrared spectroscopy

The chemical composition of the 3D scaffolds was characterized by ATR-FTIR (Fig. 2). The raw materials showed the characteristic peaks of the chemical bonds present on TCP (P═O stretch at 1200 cm^{-1}) as well as on Gel and CH (O—H, N—H (I), C—H, C═O, and N—H (II) vibrations at 3292, 1530, 2871, 1640, and 3284 cm^{-1}, respectively). Moreover, the spectra of GO present peaks associated to the O—H, C—H, C═O, C═C, and C—O vibrations at 3331, 2921, 1713, 1635, and 1073 cm^{-1}, respectively. Regarding the 3D_rGO and 3D_control scaffolds (Fig. 2B), the FTIR spectra show the presence of the main peaks attributed to each raw material, confirming their presence in the scaffolds' composition.

3.2.2. Evaluation of scaffolds' photothermal capacity

NIR-responsive photothermal therapy has been selected for application in bone tissue engineering due to the NIR light increased penetration depth in the human body [45,46]. The scaffolds' photothermal capacity was assessed under irradiation with a NIR light (808 nm, 1.7 W/cm^2) for 10 min. As observed in Fig. 2C (and Fig. S2), 3D_rGO1, 3D_rGO2, and 3D_rGO4 scaffolds generated a temperature increase of 12.3 °C, 13 °C, and 16.7 °C, respectively. In this regard, the photothermal capacity displayed by 3D_rGO scaffolds is proportional to the rGO concentration in their structure. Moreover, different works in literature demonstrated the photothermal effects within this range can accelerate the bone healing process or even provide an antibacterial

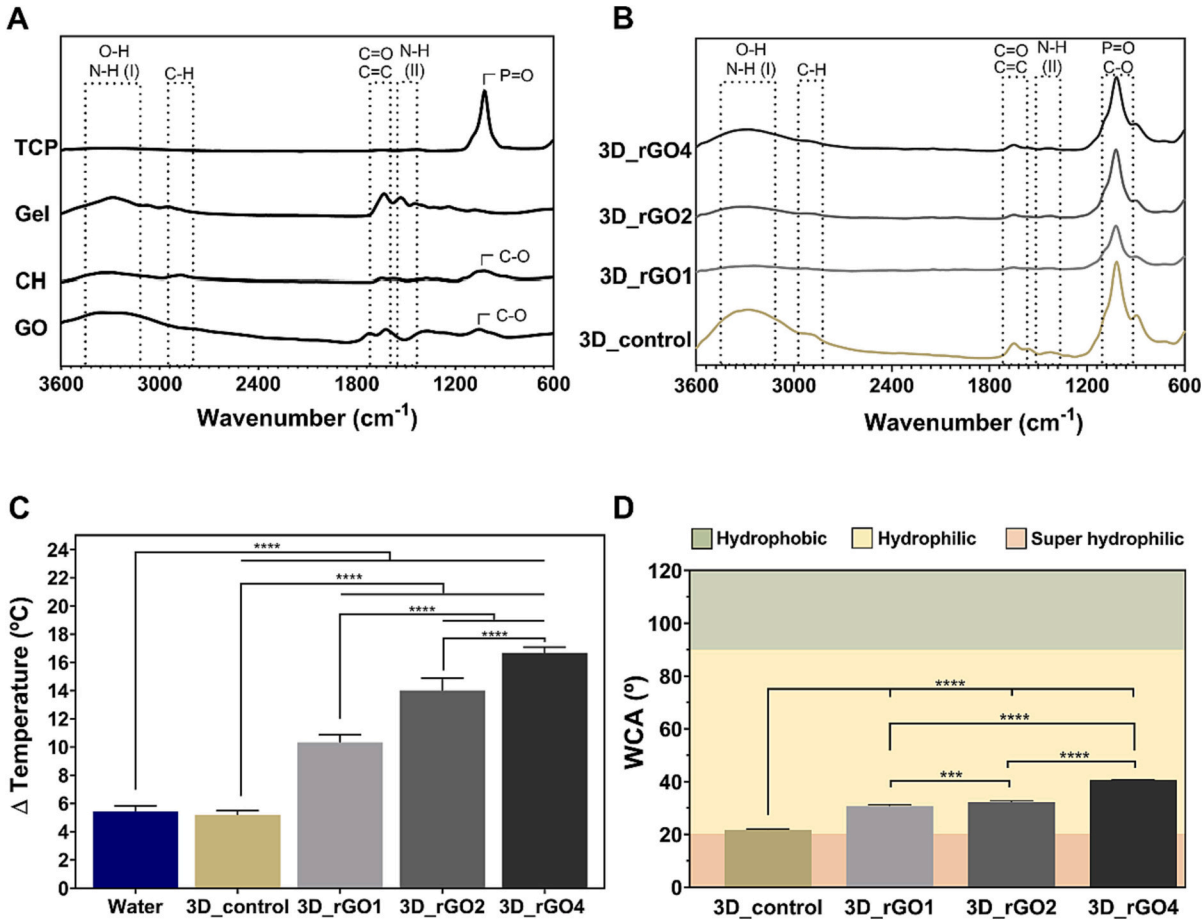

Fig. 2. Analysis of TCP, Gel, CH, and GO (A), and 3D_control and 3D_rGO scaffolds (B) by ATR-FTIR; Temperature variation of the different scaffold formulations after 10 min of NIR light irradiation (808 nm, 1.7 W/cm^2) (C). Data are presented as mean ± SD, $n = 3$ (****$p < 0.0001$); Analysis of the non-irradiated (W/O NIR) scaffolds' surface wettability (D). Data are presented as mean ± SD, $n = 3$ (***$p < 0.001$, ****$p < 0.0001$).

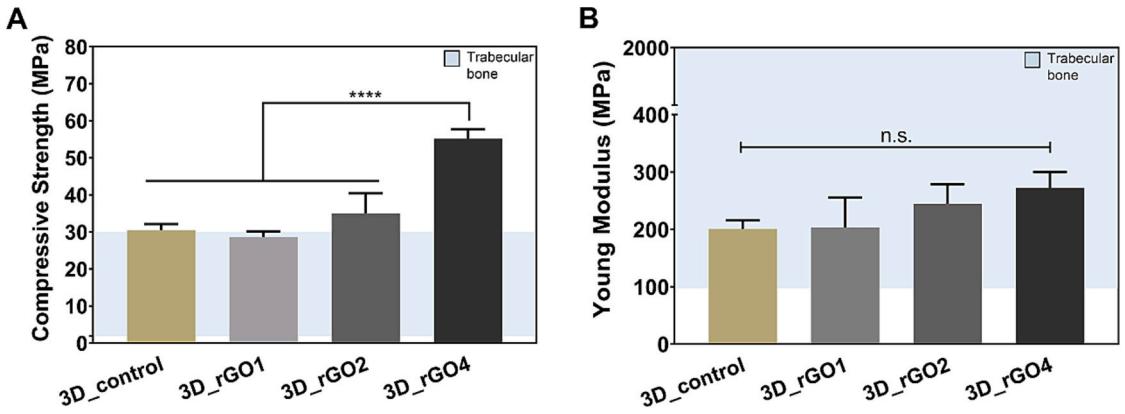

Fig. 3. Analysis of the mechanical properties of the produced 3D scaffolds. Compressive strength (A) and Young Modulus (B). Data are presented as mean ± SD, $n = 5$ (**** $p < 0.0001$, n.s. – not statistically significant).

effect [24,25,47]. In turn, 3D_control scaffolds and water (control) induced a similar temperature increase upon NIR laser irradiation (ΔT = 5 °C). Such data is coherent with the weaker interaction of 808 nm light with biological components (*e.g.* water, hemoglobin, proteins, and melanin) being indicative of the safety of this radiation [48,49].

Altogether, this data show that the 3D_rGO scaffolds' photothermal effect is dependent on the rGO concentration. Such is in accordance with data available in the literature for similar approaches. For example, Wu et al. also observed that increasing concentrations of rGO will increase the heat generated under NIR irradiation and consequently the temperature of the surrounding environment [50]. Moreover, the overall achieved temperature can also be indicative of potential therapeutic effects since local hyperthermia, over 50 °C, has been linked to high antibacterial efficacies [51–53].

3.2.3. Evaluation of the scaffolds' surface wettability

The scaffolds' wettability can affect their biological response, particularly the protein adsorption and cell adhesion. According to the literature, in comparison to hydrophobic (WCA > 90°) or super hydrophilic surfaces (WCA < 20°), the utilization of moderate hydrophilic surfaces (40° < WCA < 70°) can be advantageous for the cell adhesion processes [54,55].

The data showed that 3D_control scaffolds exhibit a WCA value of ≈ 22°, which is close to the upper limit of a super hydrophilic character (Fig. 2D). Otherwise, the incorporation of rGO changed the scaffolds' wettability, presenting an increase in the WCA with the increase in rGO concentration, *i.e.*, ≈ 30°, ≈ 32°, ≈ 41° for 3D_rGO1, 3D_rGO2 and 3D_rGO4 scaffolds, respectively. Such data can be attributed to the elimination of the oxygen-containing functional groups present on GO during the reduction process, resulting in a more hydrophobic character of rGO and 3D_rGO scaffolds. Furthermore, the incorporation and *in situ* reduction of GO resulted in WCAs closer to those considered ideal for biological interactions, with a moderate hydrophilic character. Surfaces with moderate hydrophilic character have been associated with optimal behavior when considering proteins adsorption and cell adhesion and proliferation [54,56]. Kumar and colleagues also observed that by increasing the rGO content from 1 to 3 and 5 wt%, the WCAs of PCL/rGO composites also rose from ≈ 89° for PCL/rGO_1 to ≈ 91° for PCL/rGO_3 and ≈ 93° for PCL/rGO_5 [57]. Therefore, rGO incorporation can be a straightforward approach for modulating the WCA of biomaterials, namely to provide them a moderate hydrophilic character.

3.2.4. Determination of the mechanical properties

The mechanical resistance and stability of the 3D_rGO scaffolds are crucial for determining their capacity to act as temporary supports during the bone regeneration process, *i.e.*, maintaining, replacing, and improving the bone's native functions. In this way, the mechanical properties exhibited by the scaffolds should be as similar as possible to the injured bone to avoid stress-shielding effects, which arise from the reduction of bone density (osteopenia) in response to a graft stiffer than the native bone tissue [58].

The obtained results (Fig. 3A and B) show that the 3D_rGO4 exhibits a higher compressive strength value (≈ 55 MPa), while 3D_control, 3D_rGO1, and 3D_rGO2 scaffolds presented compressive strength values

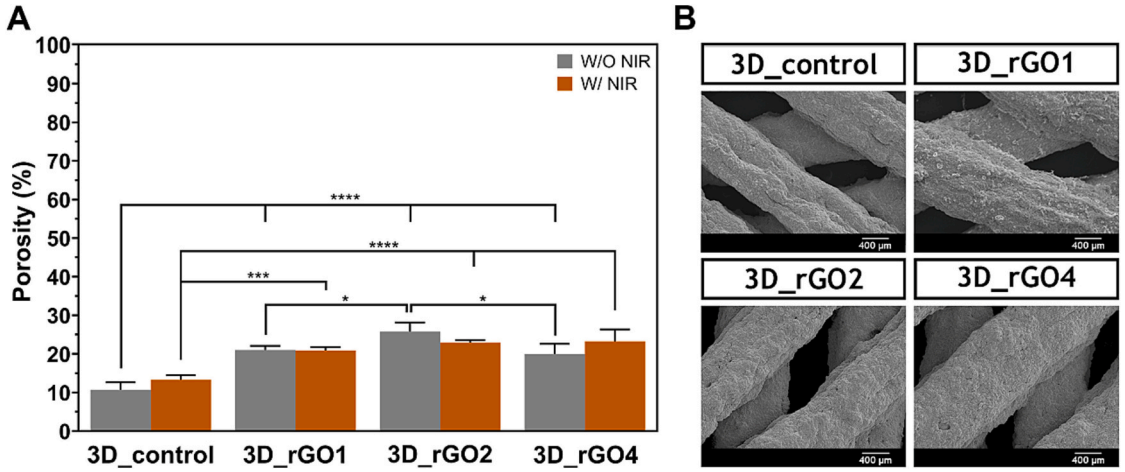

Fig. 4. Evaluation of the scaffolds' total porosity without (W/O NIR) or with (W/NIR) NIR laser irradiation (808 nm, 1.7 W/cm^2, 10 min) (A). Data are presented as mean ± SD, $n = 3$ (*$p < 0.05$, ***$p < 0.001$, ****$p < 0.0001$); Representative SEM images of the surface of non-irradiated (W/O NIR) scaffolds (B).

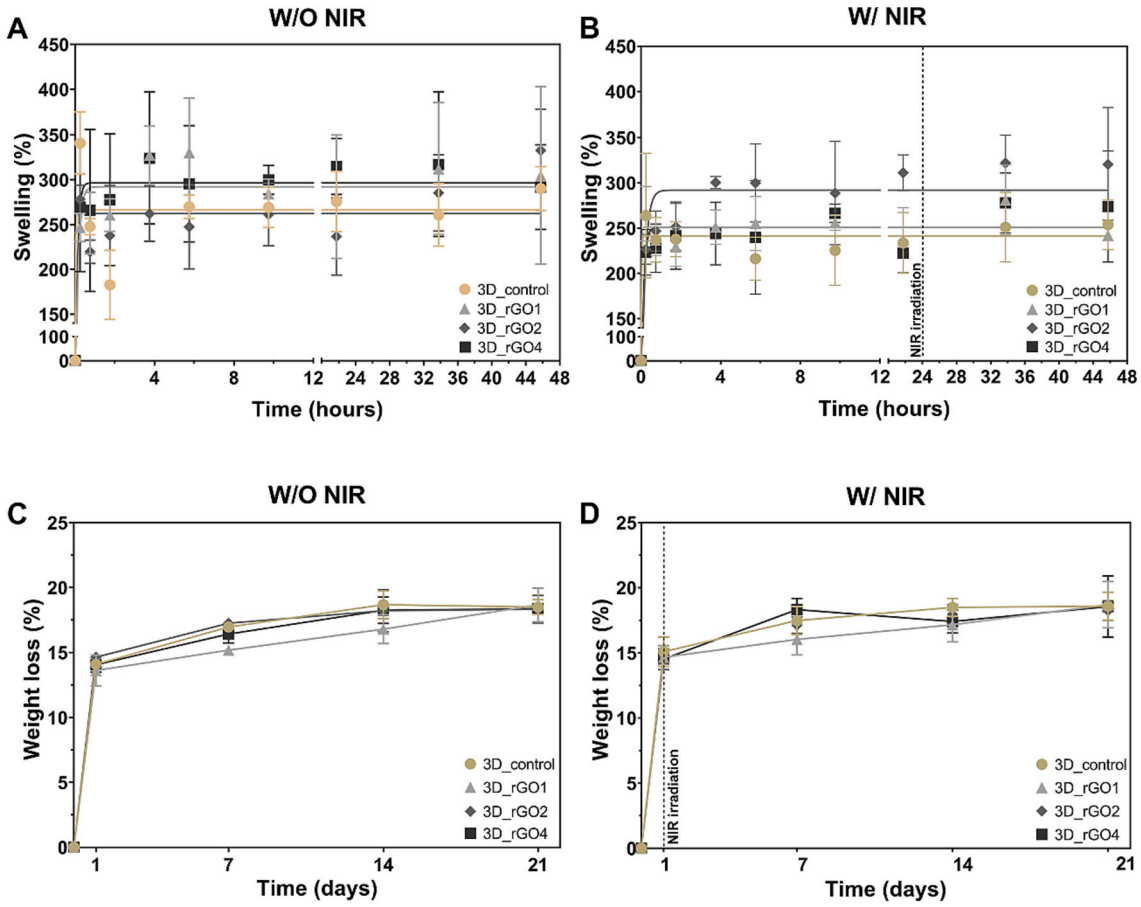

Fig. 5. Analysis of the scaffolds' swelling profile of non-irradiated (W/O NIR) (A) and irradiated (W/ NIR) scaffolds (808 nm, 1.7 W/cm^2, 10 min) (B); Determination of the scaffolds' weight loss without (W/O NIR) (C) or with (W/NIR) (D) NIR laser irradiation (808 nm, 1.7 W/cm^2, 10 min), over 21 days in PBS containing lysozyme.

of ≈ 30 MPa, ≈ 29 MPa, and ≈ 35 MPa, respectively. Such data revealed that a higher concentration of rGO confers an increased stiffness to the scaffolds, ≈ 26 MPa higher compressive strength value for 3D_rGO4 scaffolds comparatively to scaffolds with lower concentrations of rGO (*i.e.*, 3D_rGO1 and 3D_rGO2 scaffolds). In fact, different works in the literature have also reported that the incorporation of rGO on the biomaterial matrices improves the mechanical capacity and provides reinforcement for supporting the bone regeneration process, due to its large surface area [59]. Moreover, the compressive strength displayed by the produced scaffolds is within the range observed in the native trabecular bone (≈ 2–30 MPa) [60,61]. Therefore, the mechanical properties of 3D_rGO scaffolds make their preferential application in non-loading bone regions.

Furthermore, 3D_rGO4, 3D_rGO2, 3D_rGO1, and 3D_control scaffolds presented Young modulus' values of ≈ 272 MPa, ≈ 244 MPa, ≈ 204 MPa, and ≈ 201 MPa, respectively. These values are closer to those displayed by native trabecular bone (100–2000 MPa). In a comparable approach, Kumar et al. observed that PCL/rGO composites produced with higher rGO content exhibited increased storage modulus (≈ 400 MPa for PCL/rGO_1, ≈ 430 MPa for PCL/rGO_3, and 497 MPa for PCL/rGO_5) [57]. In turn, Liang and Zhang produced bone cements with different rGO contents and observed that the compressive strength increased from 28.5 MPa to 33.8 MPa, 34.1 MPa, and 35.3 MPa in cements with 0.02 %, 0.04 %, and 0.06 % of rGO, respectively [62].

3.2.5. *Determination of scaffolds' porosity*

Scaffolds' porosity, namely the pore size, overall porosity, and pore interconnectivity, influences different cellular events such as infiltration and proliferation. The pore size allows the cells' circulation to deeper areas of the scaffolds. In turn, the pores interconnectivity enables the diffusion of agents, important to the bone regeneration process, throughout the scaffolds, namely Ca^{2+} and PO_4^{3-} ions, which subsequently lead to the formation of hydroxyapatite-like layers [63,64].

The total porosity of the scaffolds (Fig. 4A) show that all formulations, with or without NIR irradiation, presented a total porosity in the range of 10–26 %. Moreover, the inclusion of rGO increased the scaffolds' porosity. Similarly, Aslan and colleagues observed that by increasing the concentration of rGO coating from 0.5, 1.0, and 1.5 wt% in P-Ti6Al4V alloys, the porosity improves to 40, 50 and 60 %, respectively [65]. Furthermore, the irradiation of NIR light did not affect the porosity of the 3D scaffolds, which is indicative of the maintenance of the scaffolds' structural integrity during the photothermal treatment. Although the scaffolds' total porosity is lower than that of the trabecular bone (50–90 %), in the literature, highly porous scaffolds with low density are often associated with sub-optimal mechanical strength [66]. Moreover, the scaffolds' macroporosity was analyzed *via* SEM images (Fig. 4B) and measured using ImageJ software. The macropore size for the different scaffold formulations was defined according to the length of the long and short axis, *i.e.*, 1148 ± 52 μm × 586 ± 96 μm for 3D_control, 1195 ± 98 μm × 554 ± 48 μm for 3D_rGO1, 1462 ± 222 μm × 650 ± 97 μm for 3D_rGO2 and 1563 ± 274 μm × 685 ± 106 μm for 3D_rGO4. This macropore size allows the internalization of osteoblast cells, which have ≈ 10–50 μm, and promotes the cells' ingrowth and regeneration of mineralized bone tissue [67–69]. Moreover, it is worth noticing that despite allowing the ingrowth of unmineralized osteoid tissue, smaller pores can occlude more easily, difficulting nutrients and gaseous exchanges as well as neovascularization [66,70]. Thus, the obtained values of porosity and microporosity are compatible with the

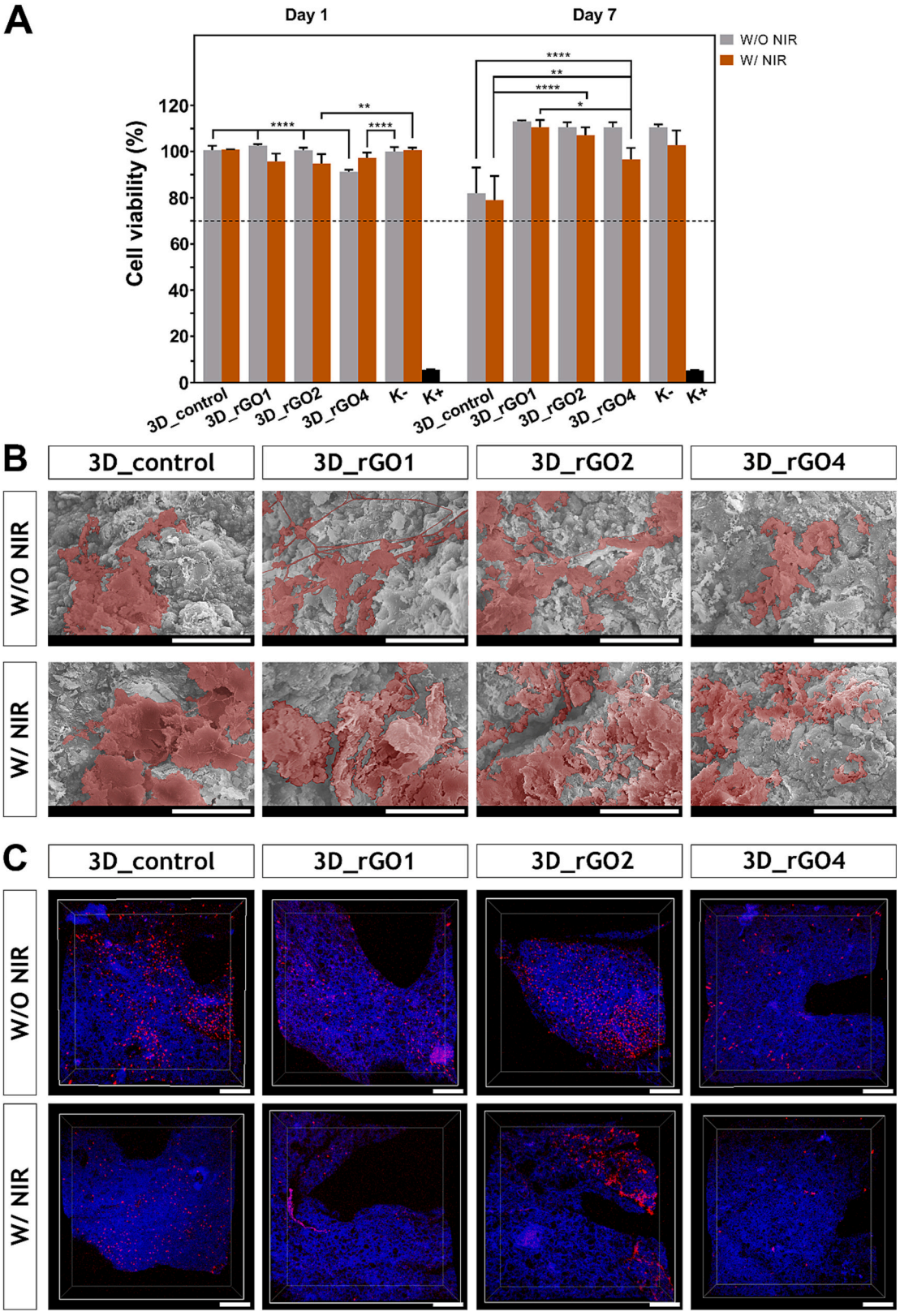

Fig. 6. Analysis of the scaffolds' cytocompatibility without (W/O NIR) or with (W/ NIR) NIR laser irradiation (808 nm, 1.7 W/cm^2, 10 min). Evaluation of the 3D scaffolds' cytotoxic profile through the resazurin assay at days 1 and 7. (K^-) negative and (K^+) positive control were used as viable and dead cells, respectively (A). Data are presented as mean ± SD, $n = 5$ (*$p < 0.05$, **$p < 0.01$, ****$p < 0.0001$); Representative pseudo-colored SEM images of hOB cells cultured onto the scaffolds' surface, over a period of 3 days. Scale bars correspond to 40 μm (B); CLSM images of the internalization of hOB cells within scaffolds without (W/O NIR) or with (W/ NIR) NIR irradiation (808 nm, 1.7 W/cm^2, 10 min), after 3 days of incubation. Scale bars correspond to 50 μm (C).

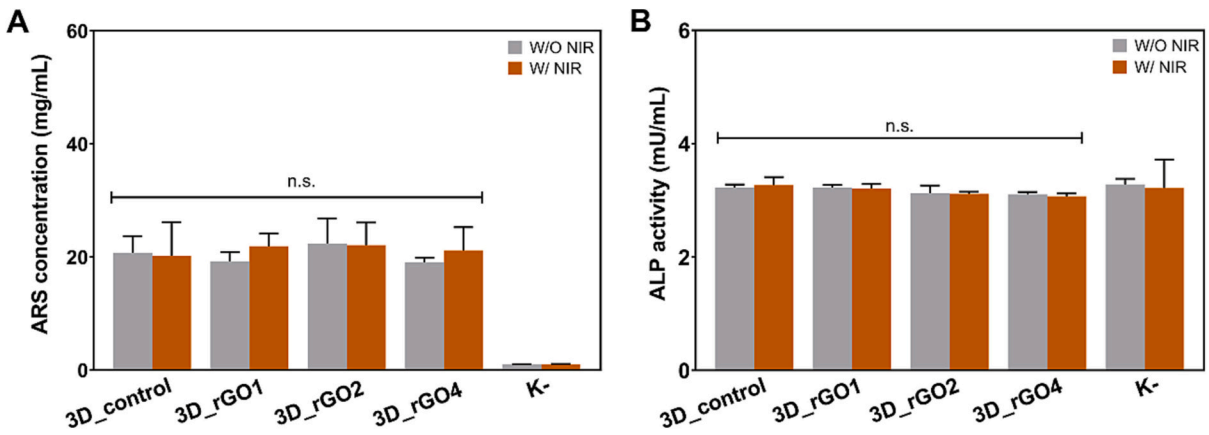

Fig. 7. Characterization of the osteogenic properties of the produced scaffolds. Analysis of the Alizarin Red concentration in the 3D scaffolds cultured with hOB cells for 14 days, without (W/O NIR) or with (W/ NIR) NIR irradiation (808 nm, 1.7 W/cm^2, 10 min) (A). Data are presented as mean ± SD, $n = 6$ (n.s. – not statistically significant); Determination of the ALP activity in hOB cells cultured with 3D_control or 3D_rGO scaffolds for 7 days, without (W/O NIR) or with (W/NIR) NIR irradiation (808 nm, 1.7 W/cm^2, 10 min). Data are presented as mean ± SD, $n = 6$ (n.s. – not statistically significant) (B).

cells' infiltration, gases and biomolecules exchanges, as well as the ingrowth of new blood vessels [66,67].

3.2.6. *Characterization of the scaffolds' swelling profile*

Scaffolds' swelling ability is important for the biological performance and formation of bone tissue. The swelling capacity indicates the scaffolds' capacity to absorb fluids, which can lead to the expansion of the polymeric matrix and facilitate the cellular internalization and diffusion of molecules and nutrients within the scaffolds' structure. Moreover, the changes in the scaffolds' structure and size during the swelling process, when excessive can lead to the loss of the scaffolds' mechanical integrity and impact on the degradation rate. Furthermore, excessive swelling and scaffold expansion can also provoke compressive stress and damage to the surrounding tissue.

The scaffolds' swelling ability was determined by immersion in PBS for ≈ 48 h without (W/O NIR) or with (W/NIR) NIR laser irradiation (Fig. 5A and B, respectively). All formulations exhibited similar behavior, achieving a plateau phase (250–300 %) after a fast swelling in the first 2 h. Moreover, these data also support the previous indication of the scaffolds' structural integrity even under irradiation with NIR light.

3.2.7. *Analysis of the scaffolds' biodegradation profile*

The successful application of the 3D scaffolds as provisional matrices for bone regeneration is highly dependent on their biodegradation profile. In this type of application, the degradation profile must be proportional to the rate of formation of the new tissue, without affecting the stability of the 3D scaffold or the integrity of the newly formed tissue, to ensure proper bone regeneration and remodeling. Moreover, the degradation products must be biocompatible and metabolized or eliminated by the organism [71,72]. Herein, the degradation of the 3D_rGO scaffolds was analyzed in PBS media supplemented with lysozyme, an enzyme found in different parts of the human body and responsible for the hydrolysis of the glycosidic bond in the chitosan backbone [73]. On the other side, gelatin macromolecular chains are easily hydrolyzed in water due to its polar functional groups. In turn, the TCP degradation in the human body is mediated by the adjacent cells, and its by-products are metabolized during the bone resorption, whereas rGO may suffer urinary and fecal excretion [74–78].

Upon one day of incubation, an initial weight loss of ≈14 % was observed for all groups, independently of the presence or absence of NIR light irradiation (Fig. 5C and D). However, the scaffolds' degradation progressively stabilized, with no formulation showing losses superior to 19 % of their initial weight, over the 21 days. These results revealed that scaffolds are suitable to act as a temporary support for bone regeneration applications. Moreover, the heat generated by NIR light did not degrade the 3D scaffolds' structure, ensuring its stability and integrity.

3.3. *Evaluation of the scaffolds' biological properties*

3.3.1. *Analysis of the scaffolds' cytocompatibility*

The cytocompatibility of the 3D_rGO scaffolds was evaluated in the presence of hOB cells, which are involved in the synthesis of bone matrix and participate in the mineralization process, through the resazurin assay [79]. Fig. 6A shows that hOB cells remain viable when in contact with the scaffolds, for 7 days which confirms the cytocompatibility of the produced scaffolds without (W/O NIR) and with (W/NIR) NIR light irradiation. These results are also indicative of the biosafety of the degradation byproducts. Furthermore, the SEM images demonstrate that hOB cells can adhere and spread at the scaffolds' surface, and the NIR irradiation was not detrimental to the cell adhesion process (Fig. 6B). Moreover, the migration and internalization of the cells in the scaffolds were also analyzed by confocal microscopy (Fig. 6C). The images show that hOB cells adhere and proliferate in the scaffolds' porous network, after 3 days of incubation. Such data demonstrate that the hOB cells not only grow at the scaffolds' surface but also in the porous interior of the scaffolds, which will enhance the deposition of new bone matrix. Overall, the increase of rGO concentration in the scaffolds and the NIR light irradiation maintained the viability and activity of osteoblasts and did not compromise the biological performance of the 3D_rGO scaffolds.

3.3.2. *Analysis of the scaffolds' biomineralization in vitro*

The deposition of minerals at the scaffolds' surface is essential for promoting the complete regeneration and maintaining the stiffness and hardness of bone tissue. Particularly, the deposition of phosphate and calcium ions prompts the nucleation of calcium phosphate crystals, namely in the form of hydroxyapatite [79]. The scaffolds' mineralization was monitored for 7 and 21 days in SBF solution and the formation of apatite crystals on the scaffolds' surface was also confirmed by SEM (Fig. S3). The images show the presence of hydroxyapatite nanocrystals at day 7, which progressively grew over 21 days to form plates in all 3D_control and 3D_rGO formulations. This can be justified by TCP's ability to stimulate the mineralization process, increasing the scaffolds'

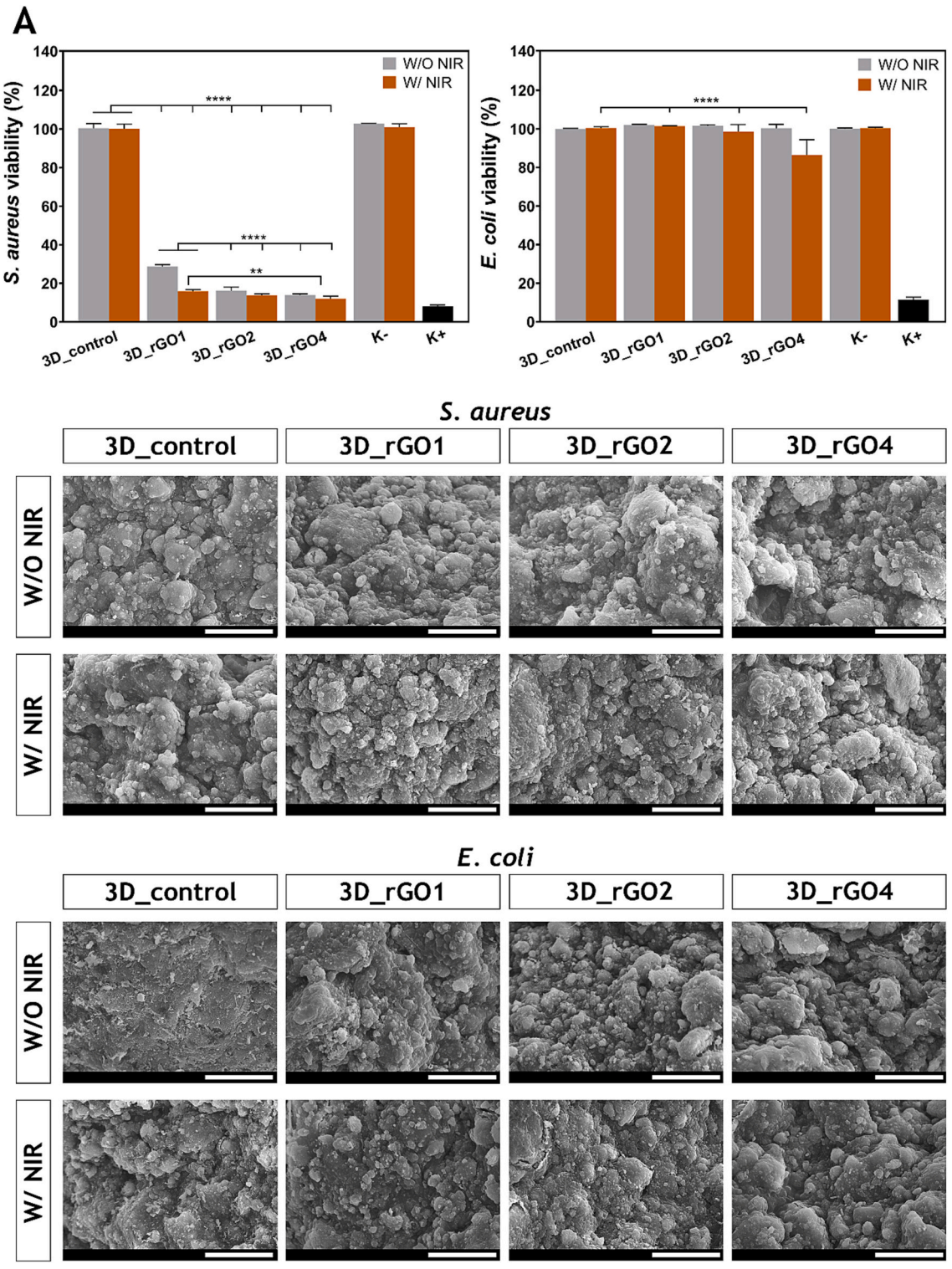

Fig. 8. Analysis of the NIR-light triggered antibacterial activity of the 3D_control and 3D_rGO formulations. Determination of the viability of *S. aureus* and *E. coli* incubated with non- irradiated (W/O NIR) and NIR light irradiated (W/ NIR; 808 nm, 1.7 W/cm^2, 10 min) scaffolds through resazurin assay (A). Data are presented as mean ± SD, $n = 5$ (**$p < 0.01$, ****$p < 0.0001$); SEM images of the surface of non-irradiated (W/O NIR) and irradiated (W/NIR; 808 nm, 1.7 W/cm^2, 10 min) scaffolds cultured in contact with *S. aureus* and *E. coli* (B). Scale bars correspond to 20 μm.

biointegration.

The mineralization of 3D_control and 3D_rGO formulations in the presence of hOB cells for 14 days was also characterized using the ARS staining (Fig. 7A). The obtained results demonstrated that the 3D_rGO1, 3D_rGO2, and 3D_rGO4 scaffolds display a similar ARS concentration to the group incubated with 3D_control scaffolds, which can be correlated to the similar hydroxyapatite deposition on all scaffold formulations. Moreover, the analysis of the ALP activity also showed that the inclusion of rGO and the NIR irradiation did not impact the activity of the hOB cells (Fig. 7B). Lee et al. also observed through ARS and ALP assays that the incorporation of rGO into HAp nanocomposites did not have a negative effect on preosteoblast cells [80]. Nevertheless, it is worth

noticing that *in vivo* assays will be essential for evaluating the osteogenic potential of the 3D_rGO scaffolds, namely the impact of mild hyperthermy in bone tissue regeneration.

3.4. Analysis of the scaffolds' antibacterial activity

Implant-related bacterial infection is one of the most frequent causes of failure for bone substitutes. These bacterial infections result in prolongated hospitalization periods, higher economic costs, and also affect the patient's quality of life. Therefore, the scaffolds' antibacterial activity was evaluated against *S. aureus* and *E. coli* (Gram-positive and Gram-negative bacteria, respectively) (Fig. 8A). Overall, the data demonstrate that the viability of *E. coli* was superior to that exhibited by *S. aureus*. Such can be attributed to the higher complexity of the cell wall in Gram-negative bacteria, which contains an additional outer lipidic membrane. The antibacterial effect of 3D scaffolds against *S. aureus* increased with the rGO concentration. The resazurin assay showed an *S. aureus* viability of ≈100 % for the 3D_control group, whereas this value decreased to ≈29 %, ≈16 %, and ≈14 % when the bacteria were incubated with 3D_rGO1, 3D_rGO2, and 3D_rGO4, respectively. Additionally, the irradiation of 3D_rGO scaffolds with NIR light (808 nm, 1.7 W/cm^2, 10 min) further increased their antibacterial activity. In the presence of NIR light, the viability of Gram-positive bacteria was ≈16 %, ≈14 %, and ≈12 %, for 3D_rGO1, 3D_rGO2, and 3D_rGO4, respectively. This can be explained by the higher rGO content and photothermal potential of the 3D_rGO4 scaffold. As expected, the irradiation of 3D_control scaffolds did not influence the viability of *S. aureus*, registering a viability of ≈100 %. Otherwise, the viability of Gram-negative *E. coli* treated with 3D_control, 3D_rGO1, 3D_rGO2, and 3D_rGO4 was ≈100 %. Upon NIR laser irradiation, the viability of *E. coli* was ≈100 % for the 3D_control, 3D_rGO1, and 3D_rGO2 groups, whereas the 3D_rGO4 group presented a viability of ≈86 %.

These results indicate that the higher concentrations of rGO confer a higher antibacterial potential to the 3D scaffolds. The antibacterial effect of rGO can be explained by two mechanisms, *i.e.*, rGO-mediated damages to bacterial cell walls by oxidizing reduced glutathione in bacteria, or through the disruption of the bacterial cell wall's integrity by sharp nano-edges of graphene nanosheets, leading to the formation of pores and to the leakage of the cytoplasmatic content [81–84]. Furthermore, rGO combined with the NIR light irradiation induced an increased antibacterial effect caused by hyperthermia. The SEM analysis also demonstrated that none of the microorganisms, *S. aureus* and *E. coli,* formed biofilms in the 3D_control or 3D_rGO scaffolds exposed to NIR light (Fig. 8B). Altogether, these results indicate that the 3D_rGO scaffolds can be explored for mediating a NIR-light antibacterial effect. Additionally, it is also important to notice that the presence of CH can also contribute to antibacterial effect exhibited by the produced 3D scaffolds. CH can disrupt bacterial growth through different mechanisms i) changes in the permeability of bacterial cell walls, ii) chelating agent, interacting with and removing traces of metals and trace elements essential for bacterial growth, and iii) formation of a polymeric envelope around the bacterial membrane, limiting nutrient absorption and intercellular exchange. However, the incorporation of CH into the 3D matrix of the scaffolds, coupled with the weight loss profile, difficults and limits the CH diffusion, which is in accordance with the antibacterial efficacy demonstrated by the 3D_control group.

4. Conclusion

Bone defects with critical size, resulting from injuries or diseases, are a major medical problem as the self-regenerative capacity of the bone is compromised. Furthermore, the limitations of traditional clinical treatments highlight the need for developing new bone substitutes based on biomimetic strategies, using biomaterials to develop personalized bone-like structures that reproduce the architecture and functions of native bone. In this work, 3D_rGO composite scaffolds, with different concentrations of rGO (1, 2, and 4 mg/mL), were produced layer-by-layer using a Fab@Home 3D Plotter printer. The incorporation of higher concentrations of rGO confers increased stiffness to the scaffolds and provides a proper reinforcement for supporting the bone regeneration process. Moreover, 3D_rGO scaffolds also exhibited physicochemical properties suitable for biological applications, namely the wettability that, with the increase in the rGO concentrations, was altered to a moderate hydrophilic character, which is in the range considered optimal for mediating the adsorption of proteins and improving cell adhesion. Furthermore, the combination of 3D_rGO scaffolds with NIR-light therapy induced a photothermal effect, generating a maximum temperature increase of 16.7 °C, which can contribute to faster bone regeneration and provide an antibacterial effect. Additionally, the 3D_rGO scaffolds also demonstrated an enhanced antibacterial potential, particularly against *S. aureus* with the increase in the rGO concentration. Moreover, the increase in the rGO concentration did not compromise the scaffolds' structural stability, biological performance, or the activity of osteoblast cells, even when irradiated with the NIR laser. Thus, the 3D_rGO4 scaffold demonstrated to be the most promising candidate for application in the treatment of traumatic bone injuries. Additionally, the incorporation of antibacterial agents, stem cells, and/or bioactive molecules (*e.g.,* growth factors and bone morphogenic proteins) may be envisioned to improve the antibacterial, osteoinductive, osteoconductive, and angiogenic properties as well as enhance the scaffolds' functionality.

CRediT authorship contribution statement

Cátia S.D. Cabral: Conceptualization, Investigation, Methodology, Writing – original draft. **Duarte de Melo-Diogo:** Conceptualization, Funding acquisition, Investigation, Writing – review & editing. **Paula Ferreira:** Investigation, Methodology, Writing – original draft. **André F. Moreira:** Conceptualization, Investigation, Methodology, Writing – original draft, Writing – review & editing. **Ilídio J. Correia:** Conceptualization, Funding acquisition, Writing – review & editing.

Declaration of competing interest

The authors declare that they have no known competing financial interests or personal relationships that could have appeared to influence the work reported in this paper.

Acknowledgments

The authors would like to thank Abílio Silva for the support in the mechanical assays. This work was developed within the scope of the CICS-UBI projects UIDB/00709/2020 and UIDP/00709/2020, financed by national funds through the Portuguese Foundation for Science and Technology/MCTES. The funding from PTDC/BTA-BTA/0696/2020 and 2022.06320.PTDC (DOI 10.54499/2022.06320.PTDC) is also acknowledged. The microscopy facility used in the development of this work is part of the PPBI-Portuguese Platform of BioImaging and is partially supported by the Project POCI-01-0145-FEDER-022122. Cátia S. D. Cabral is the recipient of a doctoral fellowship from FCT (UI/BD/151024/2021) under the scope of the CICS-UBI Programmatic Funding. Duarte de Melo-Diogo acknowledges the Foundation for Science and Technology for financial support given through a Junior Researcher contract (2021.00590.CEECIND; DOI 10.54499/2021.00590.CEECIND/CP1661/CT0001).

Appendix A. Supplementary data

Supplementary data to this article can be found online at https://doi.org/10.1016/j.ijbiomac.2024.129210.

References

[1] R. Florencio-Silva, G.R.D.S. Sasso, E. Sasso-Cerri, M.J. Simões, P.S. Cerri, Biology of bone tissue: structure, function, and factors that influence bone cells, Biomed. Res. Int. 2015 (2015).

[2] A. Wawrzyniak, K. Balawender, Structural and metabolic changes in bone, Animals 12 (15) (2022) 1946.

[3] G. Zhu, T. Zhang, M. Chen, K. Yao, X. Huang, B. Zhang, Y. Li, J. Liu, Y. Wang, Z. Zhao, Bone physiological microenvironment and healing mechanism: basis for future bone-tissue engineering scaffolds, Bioact. Mater. 6 (11) (2021) 4110–4140.

[4] N. Su, J. Yang, Y. Xie, X. Du, H. Chen, H. Zhou, L. Chen, Bone function, dysfunction and its role in diseases including critical illness, Int. J. Biol. Sci. 15 (4) (2019) 776.

[5] V. Campana, G. Milano, E. Pagano, M. Barba, C. Cicione, G. Salonna, W. Lattanzi, G. Logroscino, Bone substitutes in orthopaedic surgery: from basic science to clinical practice, J. Mater. Sci. Mater. Med. 25 (2014) 2445–2461.

[6] W. Wang, K.W.K. Yeung, Bone grafts and biomaterials substitutes for bone defect repair: a review, Bioact. Mater. 2 (4) (2017) 224–247.

[7] J. Ng, K. Spiller, J. Bernhard, G. Vunjak-Novakovic, Biomimetic approaches for bone tissue engineering, Tissue Eng. Part B Rev. 23 (5) (2017) 480–493.

[8] Y. Han, H. Lei, H. Kaken, W. Zhao, W. Wang, A. Wumanerjiang, W. Peng, L. Guo, L. Gu, Q. Kong, C. Zhou, L. Wang, 3D printing customized design of human bone tissue implant and its application, Nanotechnol. Rev. 11 (1) (2022) 1792–1801.

[9] S.M. Peltola, F.P. Melchels, D.W. Grijpma, M. Kellomäki, A review of rapid prototyping techniques for tissue engineering purposes, Ann. Med. 40 (4) (2008) 268–280.

[10] L. Ciocca, F. De Crescenzio, M. Fantini, R. Scotti, CAD/CAM and rapid prototyped scaffold construction for bone regenerative medicine and surgical transfer of virtual planning: a pilot study, Comput. Med. Imaging Graph. 33 (1) (2009) 58–62.

[11] X. Lin, S. Patil, Y.-G. Gao, A. Qian, The bone extracellular matrix in bone formation and regeneration, Front. Pharmacol. 11 (2020) 757.

[12] M. Özcan, D. Hotza, M.C. Fredel, A. Cruz, C.A.M. Volpato, Materials and manufacturing techniques for polymeric and ceramic scaffolds used in implant dentistry, J. Compos. Sci. 5 (3) (2021) 78.

[13] M.S. Bhargava Reddy, D. Ponnamma, R. Choudhary, K.K. Sadasivuni, A comparative of natural and synthetic biopolymer composite scaffold, Polymer 13 (7) (2021) 1105.

[14] A.A. Al-allaq, J.S. Kashan, A review: in vivo studies of bioceramics as bone substitute materials, Nano Select 4 (2) (2023) 123–144.

[15] C.S. Cabral, S.P. Miguel, D. de Melo-Diogo, R.O. Louro, I.J. Correia, Green reduced graphene oxide functionalized 3D printed scaffolds for bone tissue regeneration, Carbon 146 (2019) 513–523.

[16] M.H. Norahan, M. Amroon, R. Ghahremanzadeh, N. Rabiee, N. Baheiraei, Reduced graphene oxide: osteogenic potential for bone tissue engineering, IET Nanobiotechnol. 13 (7) (2019) 720–725.

[17] S. Bahrami, N. Baheiraei, M. Shahrezaee, Biomimetic reduced graphene oxide coated collagen scaffold for in situ bone regeneration, Sci. Rep. 11 (1) (2021) 16783.

[18] K. Zhou, P. Yu, X. Shi, T. Ling, W. Zeng, A. Chen, W. Yang, Z. Zhou, Hierarchically porous hydroxyapatite hybrid scaffold incorporated with reduced graphene oxide for rapid bone ingrowth and repair, ACS Nano 13 (8) (2019) 9595–9606.

[19] H. Nosrati, R. Sarraf-Mamoory, D.Q.S. Le, R. Zolfaghari Emameh, M. Canillas Perez, C.E. Bünger, Improving the mechanical behavior of reduced graphene oxide/hydroxyapatite nanocomposites using gas injection into powders synthesis autoclave, Sci. Rep. 10 (1) (2020) 8552.

[20] M.D. Stoller, S. Park, Y. Zhu, J. An, R.S. Ruoff, Graphene-based ultracapacitors, Nano Lett. 8 (10) (2008) 3498–3502.

[21] T.K. Gupta, B.P. Singh, R.K. Tripathi, S.R. Dhakate, V.N. Singh, O. Panwar, R. B. Mathur, Superior nano-mechanical properties of reduced graphene oxide reinforced polyurethane composites, RSC Adv. 5 (22) (2015) 16921–16930.

[22] X. Zhang, B. Tan, Y. Wu, M. Zhang, J. Liao, A review on hydrogels with photothermal effect in wound healing and bone tissue engineering, Polymers 13 (13) (2021) 2100.

[23] A.S. Gonçalves, C.F. Rodrigues, A.F. Moreira, I.J. Correia, Strategies to improve the photothermal capacity of gold-based nanomedicines, Acta Biomater. 116 (2020) 105–137.

[24] M.F. Graça, B.L. Melo, R. Lima-Sousa, P. Ferreira, A.F. Moreira, I.J. Correia, Reduced graphene oxide-enriched chitosan hydrogel/cellulose acetate-based nanofibers application in mild hyperthermia and skin regeneration, Int. J. Biol. Macromol. 229 (2023) 224–235.

[25] D. Li, W. Nie, L. Chen, D. McCoul, D. Liu, X. Zhang, Y. Ji, B. Yu, C. He, Self-assembled hydroxyapatite-graphene scaffold for photothermal cancer therapy and bone regeneration, J. Biomed. Nanotechnol. 14 (12) (2018) 2003–2017.

[26] B. Huang, G. Caetano, C. Vyas, J.J. Blaker, C. Diver, P. Bártolo, Polymer-ceramic composite scaffolds: the effect of hydroxyapatite and β-tricalcium phosphate, Materials 11 (1) (2018) 129.

[27] M. Bohner, B.L.G. Santoni, N. Döbelin, β-tricalcium phosphate for bone substitution: synthesis and properties, Acta Biomater. 113 (2020) 23–41.

[28] I.R. Serra, R. Fradique, M.C. Vallejo, T.R. Correia, S.P. Miguel, I.J. Correia, Production and characterization of chitosan/gelatin/β-TCP scaffolds for improved bone tissue regeneration, Mater. Sci. Eng. C 55 (2015) 592–604.

[29] H. Jeong, D.Y. Lee, D.H. Yang, Y.-S. Song, Mechanical and cell-adhesive properties of gelatin/polyvinyl alcohol hydrogels and their application in wound dressing, Macromol. Res. 30 (4) (2022) 223–229.

[30] D. de Melo-Diogo, C. Pais-Silva, E.C. Costa, R.O. Louro, I.J. Correia, D-α-tocopheryl polyethylene glycol 1000 succinate functionalized nanographene oxide for cancer therapy, Nanomed. 12 (5) (2017) 443–456.

[31] A.L. Torres, V.M. Gaspar, I.R. Serra, G.S. Diogo, R. Fradique, A.P. Silva, I.J. Correia, Bioactive polymeric–ceramic hybrid 3D scaffold for application in bone tissue regeneration, Mater. Sci. Eng. C 33 (7) (2013) 4460–4469.

[32] H. Jiankang, L. Dichen, L. Yaxiong, Y. Bo, L. Bingheng, L. Qin, Fabrication and characterization of chitosan/gelatin porous scaffolds with predefined internal microstructures, Polymer 48 (15) (2007) 4578–4588.

[33] R. Fradique, T.R. Correia, S.P. Miguel, K.D. De Sá, D.R. Figueira, A.G. Mendonça, I. J. Correia, Production of new 3D scaffolds for bone tissue regeneration by rapid prototyping, J. Mater. Sci. Mater. Med. 27 (69) (2016) 1–14.

[34] J.C. Boga, S.P. Miguel, D. de Melo-Diogo, A.G. Mendonça, R.O. Louro, I.J. Correia, In vitro characterization of 3D printed scaffolds aimed at bone tissue regeneration, Colloids Surf. B Biointerfaces 165 (2018) 207–218.

[35] T. Kokubo, H. Takadama, How useful is SBF in predicting in vivo bone bioactivity? Biomaterials 27 (15) (2006) 2907–2915.

[36] R. Lima-Sousa, D. de Melo-Diogo, C.G. Alves, C.S. Cabral, S.P. Miguel, A. G. Mendonça, I.J. Correia, Injectable in situ forming thermo-responsive graphene based hydrogels for cancer chemo-photothermal therapy and NIR light-enhanced antibacterial applications, Mater. Sci. Eng. C 117 (2020) 111294.

[37] P. Vashisth, J.R. Bellare, Development of hybrid scaffold with biomimetic 3D architecture for bone regeneration, Nanomedicine: Nanotechnology, Biol. Med. 14 (4) (2018) 1325–1336.

[38] C.A. Gregory, W.G. Gunn, A. Peister, D.J. Prockop, An alizarin red-based assay of mineralization by adherent cells in culture: comparison with cetylpyridinium chloride extraction, Anal. Biochem. 329 (1) (2004) 77–84.

[39] J.L. Moreau, H.H. Xu, Mesenchymal stem cell proliferation and differentiation on an injectable calcium phosphate–chitosan composite scaffold, Biomaterials 30 (14) (2009) 2675–2682.

[40] F. Ghorbani, B. Ghalandari, M. Sahranavard, A. Zamanian, M.N. Collins, Tuning the biomimetic behavior of hybrid scaffolds for bone tissue engineering through surface modifications and drug immobilization, Mater. Sci. Eng. C 130 (2021) 112434.

[41] S.P. Miguel, M.P. Ribeiro, H. Brancal, P. Coutinho, I.J. Correia, Thermoresponsive chitosan–agarose hydrogel for skin regeneration, Carbohydr. Polym. 111 (2014) 366–373.

[42] L. Vidal, C. Kampleitner, S. Krissian, M.A. Brennan, O. Hoffmann, Y. Raymond, Y. Maazouz, M.-P. Ginebra, P. Rosset, P. Layrolle, Regeneration of segmental defects in metatarsus of sheep with vascularized and customized 3D-printed calcium phosphate scaffolds, Sci. Rep. 10 (1) (2020) 7068.

[43] A.R. Calore, V. Srinivas, L. Groenendijk, A. Serafim, I.C. Stancu, A. Wilbers, N. Leoné, A.A. Sanchez, D. Auhl, C. Mota, Manufacturing of scaffolds with interconnected internal open porosity and surface roughness, Acta Biomater. 156 (2023) 158–176.

[44] S. Cai, C. Wu, W. Yang, W. Liang, H. Yu, L. Liu, Recent advance in surface modification for regulating cell adhesion and behaviors, Nanotechnol. Rev. 9 (1) (2020) 971–989.

[45] W. Zhao, Y. Zhao, Q. Wang, T. Liu, J. Sun, R. Zhang, Remote light-responsive nanocarriers for controlled drug delivery: advances and perspectives, Small 15 (45) (2019) 1903060.

[46] S. Wang, F. Wang, X. Zhao, F. Yang, Y. Xu, F. Yan, D. Xia, Y. Liu, The effect of near-infrared light-assisted photothermal therapy combined with polymer materials on promoting bone regeneration: a systematic review, Mater. Des. 217 (2022) 110621.

[47] Y.-W. Ge, X.-L. Liu, D.-g. Yu, Z.-A. Zhu, Q.-F. Ke, Y.-Q. Mao, Y.-P. Guo, J.-W. Zhang, Graphene-modified CePO4 nanorods effectively treat breast cancer-induced bone metastases and regulate macrophage polarization to improve osteo-inductive ability, J. Nanobiotechnol. 19(1) (2021) 1–17.

[48] G. Strangman, D.A. Boas, J.P. Sutton, Non-invasive neuroimaging using near-infrared light, Biol. Psychiatry 52 (7) (2002) 679–693.

[49] W. Zhang, J. Dai, G. Zhang, Y. Zhang, S. Li, D. Nie, Photothermal/pH dual-responsive drug delivery system of amino-terminated HBP-modified rGO and the chemo-photothermal therapy on tumor cells, Nanoscale Res. Lett. 13 (1) (2018) 379.

[50] J. Wu, Z. Li, Y. Li, A. Pettitt, F. Zhou, Photothermal effects of reduced graphene oxide on pancreatic cancer, Technol. Cancer Res. Treat. 17 (2018) 1533034618768637.

[51] K. Su, L. Tan, X. Liu, Z. Cui, Y. Zheng, B. Li, Y. Han, Z. Li, S. Zhu, Y. Liang, X. Feng, X. Wang, S. Wu, Rapid photo-sonotherapy for clinical treatment of bacterial infected bone implants by creating oxygen deficiency using sulfur doping, ACS Nano 14 (2) (2020) 2077–2089.

[52] Z. Wan, P. Zhang, L. Lv, Y. Zhou, NIR light-assisted phototherapies for bone-related diseases and bone tissue regeneration: a systematic review, Theranostics 10 (25) (2020) 11837–11861.

[53] X. Men, F. Wang, H. Chen, Y. Liu, X. Men, Y. Yuan, Z. Zhang, D. Gao, C. Wu, Z. Yuan, Ultrasmall semiconducting polymer dots with rapid clearance for second near-infrared photoacoustic imaging and photothermal cancer therapy, Adv. Funct. Mater. 30 (24) (2020) 1909673.

[54] S.M. Oliveira, N.M. Alves, J.F. Mano, Cell interactions with superhydrophilic and superhydrophobic surfaces, J. Adhes. Sci. Technol. 28 (8–9) (2014) 843–863.

[55] D.P. Dowling, I.S. Miller, M. Ardhaoui, W.M. Gallagher, Effect of surface wettability and topography on the adhesion of osteosarcoma cells on plasma-modified polystyrene, J. Biomater. Appl. 26 (3) (2011) 327–347.

[56] L. Chen, C. Yan, Z. Zheng, Functional polymer surfaces for controlling cell behaviors, Mater. Today 21 (1) (2018) 38–59.

[57] S. Kumar, S. Raj, E. Kolanthai, A.K. Sood, S. Sampath, K. Chatterjee, Chemical functionalization of graphene to augment stem cell osteogenesis and inhibit biofilm

formation on polymer composites for orthopedic applications, ACS Appl. Mater. Interfaces 7 (5) (2015) 3237–3252.
[58] L. Bi, W. Cheng, H. Fan, G. Pei, Reconstruction of goat tibial defects using an injectable tricalcium phosphate/chitosan in combination with autologous platelet-rich plasma, Biomaterials 31 (12) (2010) 3201–3211.
[59] L. Yu, L. Wang, W. Xu, L. Chen, M. Fu, J. Wu, D. Ye, Adsorption of VOCs on reduced graphene oxide, J. Environ. Sci. 67 (2018) 171–178.
[60] S. Bose, M. Roy, A. Bandyopadhyay, Recent advances in bone tissue engineering scaffolds, Trends Biotechnol. 30 (10) (2012) 546–554.
[61] S. Mohamed, B. Shamaz, Bone tissue engineering and bony scaffolds, Int. J. Dent. Oral Health 1 (1) (2015) 15–20.
[62] W. Liang, G. Zhang, Effect of reduced graphene oxide on the early-age mechanical properties of geopolymer cement, Mater. Lett. 276 (2020) 128223.
[63] Q.L. Loh, C. Choong, Three-dimensional scaffolds for tissue engineering applications: role of porosity and pore size, Tissue Eng. Part B Rev. 19 (6) (2013) 485–502.
[64] S.J. Hollister, Porous scaffold design for tissue engineering, Nat. Mater. 4 (7) (2005) 518–524.
[65] N. Aslan, B. Aksakal, B. Dikici, Z.A. Sinirlioglu, Graphene reinforced hybrid-bioceramic coatings on porous-Ti6Al4V for biomedical applications: morphology, corrosion resistance, and cell viability, J. Mater. Sci. 57 (35) (2022) 16858–16874.
[66] V. Karageorgiou, D. Kaplan, Porosity of 3D biomaterial scaffolds and osteogenesis, Biomaterials 26 (27) (2005) 5474–5491.
[67] N. Abbasi, S. Hamlet, R.M. Love, N.-T. Nguyen, Porous scaffolds for bone regeneration, J. Sci.: Adv. Mater. Devices 5 (1) (2020) 1–9.
[68] Q. Ran, W. Yang, Y. Hu, X. Shen, Y. Yu, Y. Xiang, K. Cai, Osteogenesis of 3D printed porous Ti6Al4V implants with different pore sizes, J. Mech. Behav. Biomed. Mater. 84 (2018) 1–11.
[69] N. Taniguchi, S. Fujibayashi, M. Takemoto, K. Sasaki, B. Otsuki, T. Nakamura, T. Matsushita, T. Kokubo, S. Matsuda, Effect of pore size on bone ingrowth into porous titanium implants fabricated by additive manufacturing: An *in vivo* experiment, Mater. Sci. Eng. C 59 (2016) 690–701.
[70] C. Luo, C. Wang, X. Wu, X. Xie, C. Wang, C. Zhao, C. Zou, F. Lv, W. Huang, J. Liao, Influence of porous tantalum scaffold pore size on osteogenesis and osteointegration: a comprehensive study based on 3D-printing technology, Mater. Sci. Eng. C 129 (2021) 112382.
[71] M.I. Echeverria Molina, K.G. Malollari, K. Komvopoulos, Design challenges in polymeric scaffolds for tissue engineering, Front. Bioeng. Biotechnol. 9 (2021) 617141.
[72] K.N. Bitar, E. Zakhem, Design strategies of biodegradable scaffolds for tissue regeneration, Biomedical Engineering and Computational Biology 6 (2014) 13–20.
[73] A. Lončarević, M. Ivanković, A. Rogina, Lysozyme-induced degradation of chitosan: the characterisation of degraded chitosan scaffolds, Journal of Tissue Repair and Regeneration 1 (2017).
[74] M. Peter, N. Ganesh, N. Selvamurugan, S.V. Nair, T. Furuike, H. Tamura, R. Jayakumar, Preparation and characterization of chitosan–gelatin/nanohydroxyapatite composite scaffolds for tissue engineering applications, Carbohydr. Polym. 80 (3) (2010) 687–694.
[75] K.D. De Sá, D.R. Figueira, S.P. Miguel, T.R. Correia, A.P. Silva, I.J. Correia, 3D scaffolds coated with nanofibers displaying bactericidal activity for bone tissue applications, Int. J. Polym. Mater. Polym. Biomater. 66 (9) (2017) 432–442.
[76] D.A. Jasim, H. Boutin, M. Fairclough, C. Ménard-Moyon, C. Prenant, A. Bianco, K. Kostarelos, Thickness of functionalized graphene oxide sheets plays critical role in tissue accumulation and urinary excretion: a pilot PET/CT study, Applied Mater. Today 4 (2016) 24–30.
[77] B.S. Dash, Y.-J. Lu, P. Pejrprim, Y.-H. Lan, J.-P. Chen, Hyaluronic acid-modified, IR780-conjugated and doxorubicin-loaded reduced graphene oxide for targeted cancer chemo/photothermal/photodynamic therapy, Biomaterials Advances 136 (2022) 212764.
[78] L. Ou, B. Song, H. Liang, J. Liu, X. Feng, B. Deng, T. Sun, L. Shao, Toxicity of graphene-family nanoparticles: a general review of the origins and mechanisms, Part. Fibre Toxicol. 13 (1) (2016) 57.
[79] H.C. Blair, Q.C. Larrouture, Y. Li, H. Lin, D. Beer-Stoltz, L. Liu, R.S. Tuan, L. J. Robinson, P.H. Schlesinger, D.J. Nelson, Osteoblast differentiation and bone matrix formation in vivo and in vitro, Tissue Eng. Part B Rev. 23 (3) (2017) 268–280.
[80] J.H. Lee, Y.C. Shin, S.-M. Lee, O.S. Jin, S.H. Kang, S.W. Hong, C.-M. Jeong, J. B. Huh, D.-W. Han, Enhanced osteogenesis by reduced graphene oxide/hydroxyapatite nanocomposites, Sci. Rep. 5 (1) (2015) 18833.
[81] S. Liu, T.H. Zeng, M. Hofmann, E. Burcombe, J. Wei, R. Jiang, J. Kong, Y. Chen, Antibacterial activity of graphite, graphite oxide, graphene oxide, and reduced graphene oxide: membrane and oxidative stress, ACS Nano 5 (9) (2011) 6971–6980.
[82] V.T.H. Pham, V.K. Truong, M.D.J. Quinn, S.M. Notley, Y. Guo, V.A. Baulin, M. Al Kobaisi, R.J. Crawford, E.P. Ivanova, Graphene induces formation of pores that kill spherical and rod-shaped Bacteria, ACS Nano 9 (8) (2015) 8458–8467.
[83] X. Chen, J. Zhou, Y. Qian, L. Zhao, Antibacterial coatings on orthopedic implants, Materials Today Bio 19 (2023) 100586.
[84] F. Naseer, E. Zahir, E.Y. Danish, M. Gull, S. Noman, M.T. Soomro, Superior antibacterial activity of reduced graphene oxide upon decoration with iron oxide nanorods, J. Environ. Chem. Eng. 8 (5) (2020) 104424.